Available online at https://link.springer.com/journal/42241
http://www.jhydrodynamics.com
Journal of Hydrodynamics, 2022, 34(2): 234-243
https://doi.org/10.1007/s42241-022-0019-2

Identification and analysis of the inlet vortex of an axial-flow pump

Wen-peng Zhang, Li-jian Shi, Fang-ping Tang*, Zhuang-zhuang Sun, Ye Zhang
College of Hydraulic Science and Engineering, Yangzhou University, Yangzhou 225009, China

(Received August 19, 2020, Revised September 4, 2020, Accepted September 8, 2020, Published online April 16, 2022)

Abstract: Axial-flow pumps are widely employed in urban flood control and drainage pumping stations. The inlet vortex is one factor that seriously threaten the safe, stable and efficient operation of axial-flow pump units. In this paper, the vortex recognition performances of two vortex identification methods, the Q-criterion and Liutex methods, are compared based on an axial-flow pump, and the interactions between the impeller and vortex are explored. A flat plate vortex generator is installed in front of the impeller to continuously induce a stable vortex. The numerical simulation results show that the Liutex method can not only simultaneously identify strong and weak vortices but also reduce the influence of shear force at the sidewall. The vortex and the impeller influence each other. Under the influence of rotating blades, the vortex changes from a low frequency to the blade frequency, and the vortex significantly changes the tangential velocity inside the impeller. The accuracy of the numerical simulation results is verified by experiments on the external and internal characteristics.

Key words: Axial-flow pump, inlet vortex, vortex identification, vortex generator, numerical simulation, experiment

Introduction

In recent years, flood disasters in southern China have become increasingly frequent, posing a great threat to people's lives and property safety in these areas. To protect against natural disasters, many cities have begun to plan and build drainage axial-flow pumping stations. Due to the large change in the water level, drainage pumping stations often deviate from the design working condition, resulting in unstable operation and other problems, and an inlet vortex is one of the important factors. An inlet vortex causes a decrease in efficiency, serious cavitation, and an increase in noise and can even cause the pump unit not to operate[1-3]. Designers try to avoid an inlet vortex during design, but it may still appear in engineering applications. A picture of an inlet vortex is shown in Fig. 1.

Fig. 1 (Color online) Picture of an inlet vortex

Since an inlet vortex was first recognized to have a negative effect on the performance of axial-flow pump, extensive research has been done on it. Rajendran et al.[4] simulated the three-dimensional turbulent flow in a water pump intake bay and validated the results by experiments. The results showed that the predicted number, location, and general structure of the vortices were in good agreement with those observed in the experiments, but the predicted vortices were generally larger and weaker than the measured vortices. Kim et al.[5] analyzed the vortex and swirl angle in the pump sump station model by methods of experimental and numerical simulation. They obtained the vortex core region by the submerged bottom vortex method and suppressed the vortex by use of an anti-vortex device. Song and Liu[6] investigated the influence of a floor-attached vortex on the pressure pulsation at a pump sump through theoretical and experimental analysis and found that the pressure pulsation induced by the floor-attached vortex fluctuates periodically with time. An inlet vortex is a typical three-dimensional unsteady flow phenomenon that is often discontinuous in time and unstable in position, which brings great difficulties to the research.

Project supported by the National Natural Science Foundation of China (Grant No. 51376155).
Biography: Wen-peng Zhang (1991-), Male, Ph. D. Candidate,
E-mail: 18852727757@163.com
Corresponding author: Fang-ping Tang
E-mail: Tangfp@yzu.edu.cn

Therefore, to reveal the change trend of an inlet vortex in an impeller, a stable vortex must be generated. Vortex generators (VGs) are often used to control flow fields in research on airfoils and heat transfer[7-9]. Recently, some scholars have also applied this technology in hydraulic turbine research. Tian et al.[10-11] studied the application of VGs by numerical simulations and experiments based on a model draft tube, and the results showed that choosing the optimal VG parameters can effectively increase the static pressure recovery coefficients and working stability. Existing research results fully show the control effect of a VG. In this paper, a plate is installed in front of the impeller to induce an inlet vortex.

Although the mechanism of inlet vortex formation and elimination is widely studied, the propagation and evolution of a vortex in an impeller are rarely examined. Because the impeller rotates at a high speed, with the small space limitation, obtaining the shape of the vortex in the impeller by high-speed photography and other experimental methods is difficult. Many scholars have made great efforts to effectively identify vortex structures, and some vortex recognition methods have been proposed. Hunt et al.[12] used a numerical simulation method to develop suitable criteria for defining eddying or vortical zones, and a set of objective criteria was found that describe regions in which the streamlines circulate, converge or diverge and form high streams of high velocity flow. Liu et al.[13] proposed the Ω-method based on the idea that vorticity overtakes deformation in a vortex. With the development of many studies, Liutex/Rortex was proposed as a new method[14]. Zhang et al.[15-16] introduced the recent progress in the vortex identification methods with a focus on the newly proposed omega method and noted that the new omega method could be successfully applied to vortex identification in reversible pump turbines. In recent years, many achievements[17-19] have been made in vortex identification research; however, few studies have been performed on the vortex identification criteria for the impeller of an axial-flow pump. To reveal changes in the vortex and their influence on the flow field, the applicability of the identification method of a vortex in an impeller is worth studying.

In this paper, based on an axial-flow pump, the recognition performances of the vortex identification criteria in the rotation domain and the static domain are verified, and the interaction between the inlet vortex and the impeller is revealed. First, the accuracy of the numerical simulation is verified by experiments on the external and internal characteristics. Then, a flat VG is installed at the front of the impeller to generate a stable inlet vortex. Finally, the vortex identification performances of the Q-criterion and Liutex method in the pump are compared, and the effects of the rotating impeller and vortex evolution are analyzed.

1. Vortex identification methods

To study the effect of a vortex on pump performance, the primary step is to accurately identify and extract the vortex structure from the flow field. In this paper, we compare and analyze the performances of the Q-criterion and Liutex vortex identification methods in an impeller. As the velocity gradient tensor is independent of the Galilean frames of reference, these two methods are Galilean invariant[20].

The characteristic polynomial equation of the velocity gradient tensor $\nabla \boldsymbol{u}$ can be given by the following formula

$$\lambda^3 - P\lambda^2 + Q\lambda - R = 0 \tag{1}$$

where λ is the eigenvalue of $\nabla \boldsymbol{u}$, P, Q and R are the first, second and third invariants of $\nabla \boldsymbol{u}$, respectively.

The Q-criterion borrows the definition of the second invariant of the velocity gradient tensor. For an incompressible flow, the trace of $\nabla \boldsymbol{u}$ is 0. Thus, Q can be simplified as

$$Q = \frac{1}{2}(\Omega^2 - S^2) \tag{2}$$

where the $\| \ \|$ notation stands for the Frobenius norm of a tensor. Ω and S are defined by

$$\|\Omega\| = \sqrt{\mathrm{tr}(\Omega^{\mathrm{T}}\Omega)} \tag{3}$$

$$\|S\| = \sqrt{\mathrm{tr}(S^{\mathrm{T}}S)} \tag{4}$$

where $Q > 0$ represents the existence of a vortex, thus the Q criterion defines vortices as areas where the vorticity magnitude is greater than the magnitude of the strain rate.

The Liutex represents the local fluid rotation, and precise definitions can be obtained from Refs. [21-23], summarized here as follows:

(1) Determine the direction of Liutex vector $\boldsymbol{r}$

If the velocity gradient tensor $\nabla \boldsymbol{u}$ has three real eigenvalues, then the fluid motion contains stretching and deformation but no rotational motion. In this condition, the magnitude of the Liutex vector is zero. If $\nabla \boldsymbol{u}$ has one real and two conjugate complex eigenvalues, then there exists a vortex in this local

region. The Liutex vector is aligned in the direction of the eigenvector corresponding to the only real eigenvalue. The normalized eigenvector is denoted $\boldsymbol{r}$.

(2) Calculate the magnitude of Liutex vector R

First, rotate the initial coordinate system xyz to a new coordinate system XYZ with a transform matrix $\boldsymbol{Q}$, where the initial z-axis is rotated to the direction of $\boldsymbol{r}$. After rotation, the velocity gradient tensor becomes

$$\nabla \boldsymbol{U} = \boldsymbol{Q}\nabla \boldsymbol{u}\boldsymbol{Q}^{\mathrm{T}} = \begin{bmatrix} \dfrac{\partial U_X}{\partial X} & \dfrac{\partial U_X}{\partial Y} & 0 \\ \dfrac{\partial U_Y}{\partial X} & \dfrac{\partial U_Y}{\partial Y} & 0 \\ \dfrac{\partial U_Z}{\partial X} & \dfrac{\partial U_Z}{\partial Y} & \dfrac{\partial U_Z}{\partial Z} \end{bmatrix} \tag{5}$$

where (U_X, U_Y, U_Z) is the velocity component in XYZ coordinates.

Then, by a second transformation with matrix $\boldsymbol{P}$ the Z-axis is rotated by θ, define $\boldsymbol{P}$ as

$$\boldsymbol{P} = \begin{bmatrix} \cos\theta & \sin\theta & 0 \\ -\sin\theta & \cos\theta & 0 \\ 0 & 0 & 1 \end{bmatrix} \tag{6}$$

The velocity gradient tensor becomes

$$\nabla U_P = P\nabla U P^{\mathrm{T}} \tag{7}$$

The rotating angle θ is calculated to ensure that the absolute value of $\partial U_X / \partial Y|_\theta$ is minimal. The magnitude of the Liutex vector is then given by

$$R = 2(\beta - \alpha), \quad \beta^2 > \alpha^2 \tag{8a}$$

$$R = 0, \quad \alpha^2 \geq \beta^2 \tag{8b}$$

in which

$$\alpha = \frac{1}{2}\sqrt{\left(\frac{\partial U_Y}{\partial Y} - \frac{\partial U_X}{\partial X}\right)^2 + \left(\frac{\partial U_Y}{\partial X} + \frac{\partial U_X}{\partial Y}\right)^2} \tag{9}$$

$$\beta = \frac{1}{2}\left(\frac{\partial U_Y}{\partial X} - \frac{\partial U_X}{\partial Y}\right) \tag{10}$$

(3) Obtain the Liutex vector by $\boldsymbol{R} = R\boldsymbol{r}$

After the two coordinate rotations, the expression seems too complex. Wang et al.[24] gave an explicit formula of the Liutex vector

$$R = \left(\langle \omega, r\rangle - \sqrt{\langle \omega, r\rangle^2 - 4\lambda_{ci}^2}\right) r \tag{11}$$

2. Numerical simulation

2.1 *Research objectv*

This study is based on an axial-flow pump segment. The calculation domains include inlet straight pipe, VG, impeller, guide vane, outlet elbow and outlet straight pipe. The number of impeller blades is four, and the number of guide vane blades is five. The diameter of the impeller is 150 mm, and the rotation speed is 1 450 rpm. The design flow (q_d) of the pump is 45 L/s. The simulation model of the axial-flow pump segment is shown in Fig. 2.

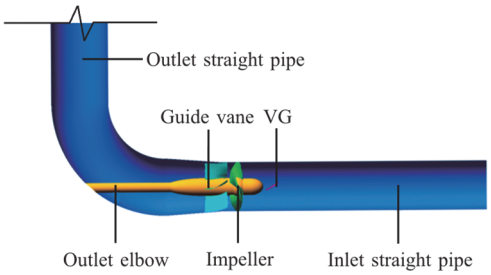

Fig. 2 (Color online) Simulation model of the axial-flow pump segment

To analyze the interaction between the vortex and impeller blade and the influence of the rotation domain on the vortex shape, three schemes are calculated, and the differences among them are shown in Table 1.

Table 1 Difference among simulation schemes

Schemes	VG	Blade of guide vane	Blade of impeller	Rotate domain
F_1	No	Yes	Yes	Yes
F_2	Yes	Yes	Yes	Yes
F_3	Yes	No	No	No

The difference between F_1 and F_2 lies in the presence or absence of the VG. The difference between F_2 and F_3 is that the impeller position is set to the static domain in F_3, in which the impeller and guide vane both do not have blades.

To generate a controllable vortex into the impeller, a flat plate VG is installed at $0.6D$ in front of the impeller center. The installation form of the VG is shown in Fig. 3, and each parameter value is shown in Table 2.

(a) (b)

Fig. 3 (Color online) Installation form of the VG

Table 2 Parameters of the VG

Parameter	Value
l /m	0.04
s /m	0.05
w /mm	4
β /°	60

2.2 *Numerical simulation method*

In this work, ANSYS CFX is utilized for the flow field calculation, and the flow is governed by the RANS equations for the numerical simulation of a three-dimensional incompressible turbulent flow in pump devices. The SST-CC model is applied for this simulation, which has been extensively tested on a wide range of both wall-bounded and free shear turbulent flows with system rotation and/or streamline curvature[25].

The inlet pipe, VG, outlet elbow and outlet straight pipe were divided into hexahedral structured grids using ICEM software. The impeller and guide vane were divided into hexahedral structured grids using TurboGrid software. Many studies have shown that the tip clearance of the impeller greatly influences the external characteristics and the internal flow field[26-27] and the tip clearance was set to 0.1 mm in this paper. The y^+ value[28] for the wall of the impeller was calculated to be 25 in post processing. The boundary layer grids of the impeller and VG were encrypted, and the meshes of the impeller and VG are shown in Fig. 4.

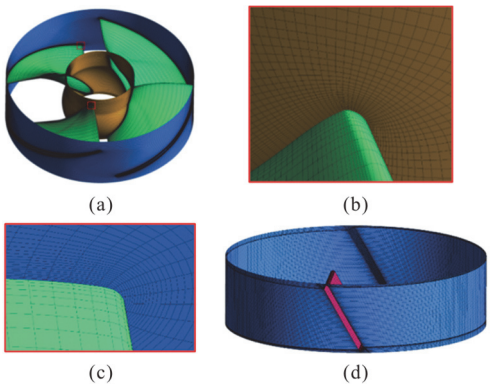

(a) (b) (c) (d)

Fig. 4 (Color online) Meshes of the impeller and VG

2.3 *Grid independence analysis*

Under the design flow rate, the head and efficiency of the pump segment were verified by a grid independence analysis, the results are shown in Fig. 5.

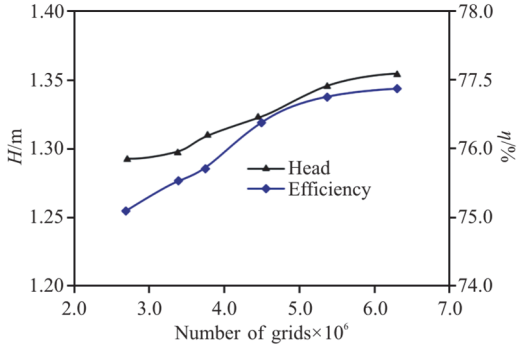

Fig. 5 (Color online) Grid independence analysis for the pump segment

For Fig. 5, the head and efficiency were calculated at 6 grid scales. With increasing number of grids, the head and efficiency of the pump segment both increase, and the trends are basically the same. When the grid number is 6.30×10^6, the head and efficiency increase by 0.07 m, 1.79%, respectively, compared to when the grid number is 2.69×10^6. When the grid number is 5.35×10^6, the grid size continues to increase, but the efficiency only increases by 0.08%. To ensure the accuracy of the calculation and save computing resources, the total number of grids in this study was set to approximately 5.35×10^6.

The entire axial-flow pump segment was first simulated as the steady computational domain. The impeller was set to the rotation domain, and the other calculation fields were set to the stationary calculation domain. The calculated flow varied from $0.7q_d$ to $1.1q_d$. Then, the q_d result was taken as the initial field for the unsteady calculation. The boundary conditions of the inlet mass flow rate and outlet static pressure were set. All the solid wall surfaces adopted no-slip wall conditions. The interface between the rotation domain and stationary domains was set to the dynamic-static calculation domain interface, the type was set to the frozen rotor type, and the other interfaces were set to the static-static calculation domain interface. In the unsteady calculation, the impeller was rotated 2° at each time step, 8 cycles were calculated, and the total time was approximately 0.331 s.

3. Validation of the numerical simulation

3.1 *Introduction of the experimental bench*

To verify the accuracy of the numerical simula-

tion, based on scheme F_1, external characteristics and laser Doppler velocimetry (LDV) measurements of the pump were performed on a hydraulic mechanical experimental bench. The vertical closed cycle system and the measurement points of the LDV experiment are shown in Fig. 6.

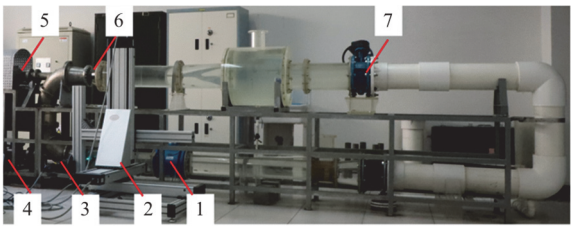

(a) Vertical closed cycle system

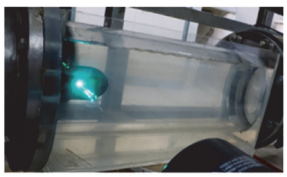

(b) Measurement points of the LDV experiment

Fig. 6 (Color online) Photo of the experimental device (1–Electromagnetic flowmeter, 2–Three-axis traverse controller, 3–Fiberoptic probes, 4-Torque meter, 5–Motor, 6–Auxiliary pump, 7–Flow control valve)

In this study, the discharge was measured by an electromagnetic flowmeter (DN 150) that had an uncertainty of ±0.2%, the head was measured by a differential pressure transmitter (EJA 110A) that had an uncertainty of ±0.1%, and the shaft power was measured by a rotary torque meter (ZJ 10) that had an uncertainty of ±0.2%. According to Eqs. (12), (13), the external characteristics can be obtained.

$$\eta = \frac{\rho g q H}{N} \times 100\% \tag{12}$$

$$N = \frac{\pi}{30} n(M - M') \tag{13}$$

where η is the efficiency, q is the flow rate, H is the head, ρ is the water density in the experiment, g is the local acceleration of gravity, N is the input power, n is the rotation speed in the experiment, M is the input torque and M' is the mechanical loss torque.

3.2 *Verification of external characteristics*

The sustained data collection time was 100 s, and the collection results were processed on average. A comparison of the external pump characteristics between the experiment and numerical simulation is shown in the Fig. 7.

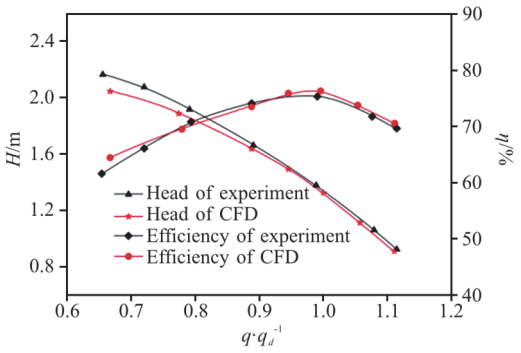

Fig. 7 (Color online) External characteristics comparison between the experiment and numerical simulation

Figure 7 shows that the numerical simulation is in agreement with the experimental external characteristics results overall, while the error is larger when the flow rate is less than $0.8q_d$. The reason for the error at small flows may be that the internal flow pattern is relatively disordered, and the experimental conditions are not identical to the numerical simulation conditions. Under the design conditions, the error in the head is less than 3%, and the error in the efficiency is less than 0.5%.

3.3 *Internal characteristic verification*

The axial velocity of the impeller inlet were measured by LDV. For the LDV measurement, the light source was an argon ion laser with a maximum power of 2 W operating in multiline mode. An optical probe with a lens was mounted on a three-axis traverse controller to place the probe volume at the location of interest. Through phase-locked technology, the variation in the velocity with impeller rotation could be measured at the measurement points, and at each measurement point, 5 000 data points were obtained. The position of a measurement point is denoted by L, with L defined as follow

$$L = \frac{L_0 - L_1}{L_2 - L_1} \tag{14}$$

where L_0 is the radius of the measurement point, L_1 is the radius of the hub and L_2 is the radius of the shroud

When the measurement point is $0.2D$ in front of the impeller center, the average axial velocity is obtained. In the numerical simulation results, the same measurement points as in the experiment are taken, and the velocity comparison is shown in Fig. 8.

Figure 8 shows that the average axial velocity near the middle of the tube is large, approximately 3 m/s, while the velocity near the sidewall suddenly

decreases and approaches 0 m/s because of the stationary sidewall. The error between the numerical simulation and LDV measurement along the whole measurement line is small except near both sidewalls, and the results of the numerical simulation are slightly larger than those of LDV. The reason for these errors may be that the boundary conditions assumed in the numerical simulation are not exactly the same as those in the experiment, and the sidewalls in the experiment are rougher than those in the numerical simulation. In the LDV experiment, the velocities of multiple periods are superimposed by phase-locked technology, while the numerical simulation covers one period. In addition, LDV measures the velocity of tracer particles, which are slightly different from the actual flow, and light refraction is inevitable when a laser passes through plexiglass.

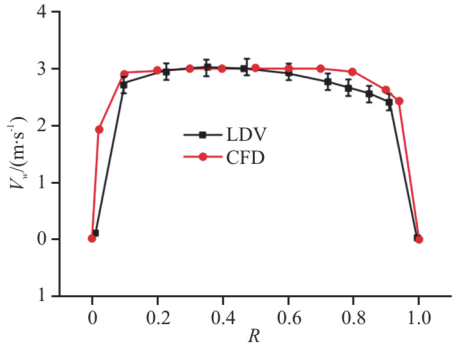

Fig. 8 (Color online) Comparison between the numerical simulation and LDV experiment

From the comparison results of the external characteristics and internal flow field, because the study is based on the design conditions, the simulation errors in the head and efficiency are all small, the velocities of the internal flow are basically consistent, and the numerical simulation results can be considered accurate.

4. Results and discussion

4.1 *Vortex identification results*

The impeller with four blades rotates periodically at a uniform speed, and each blade can be considered to have the same interference with the vortex. The interaction between a blade and the vortex is analyzed by taking a blade rotating 90° as a period. To identify the vortex by the Q-criterion and Liutex methods, and the results are shown in Fig. 9.

Figure 9 shows that the vortex shapes obtained by the two vortex identification methods are similar. A pair of vortices formed after the VG, one of which is stronger and the other weaker. The stronger vortex

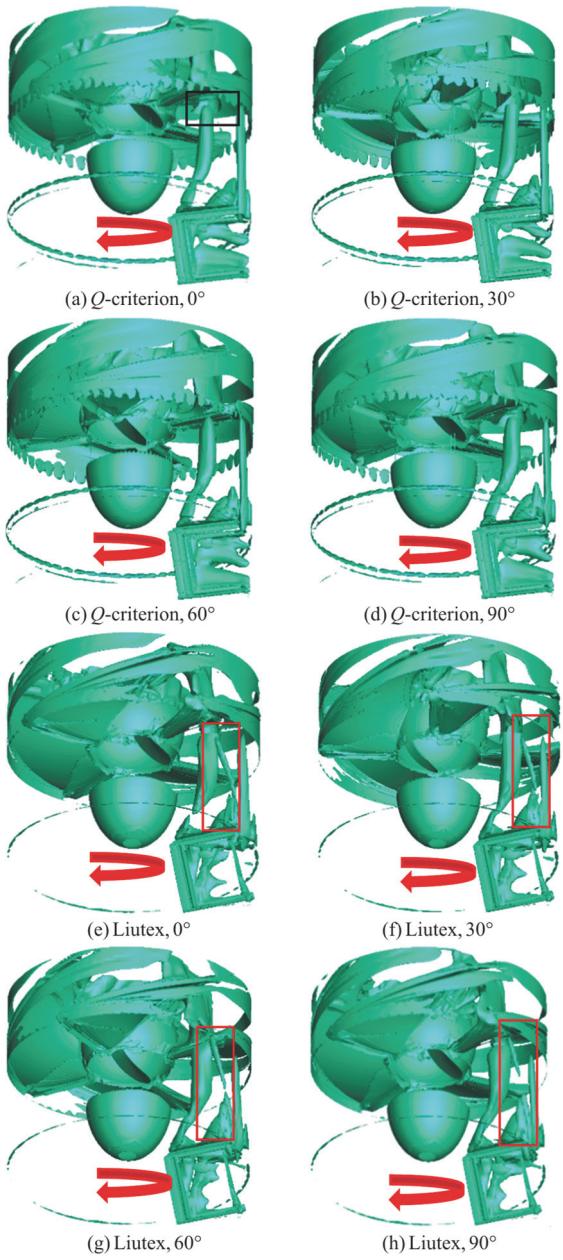

Fig. 9 (Color online) Comparison of the two vortex identification methods under different blade positions

appears on the inner side of the VG, extends to the inside of the impeller and continues to spread backward after being cut off by the blade. In contrast, the weaker vortex appears on the outer side of the VG, extends upward in the shape of a vertical vortex tube and then disappears at the inlet of the impeller. With rotation of the blade, the vortex shape before entering the impeller is basically the same. With rotation of the blade, the vortex in the impeller is cut off by the blade but still maintains the shape of the vortex tube. Comparing the two kinds of vortex identification method, the wall of the vortex tube identified by the

Q - criterion is smoother, however, there is more shear interference near the solid wall, which makes the vortex blur in the field of view. The Liutex method can identify not only the twisted change in the vortex shape due to blade rotation but also the weaker vortex, which is marked in the figure by a red rectangle.

The vortex exhibits obvious fracture at the dynamic-static interface (marked in Fig. 9(a) by a black rectangle). This may be caused by setting of the rotation domain in the numerical simulation, but in reality, this situation will not occur. To verify this conjecture, the vortex without impeller and guide vane blades is taken, as shown in Fig. 10.

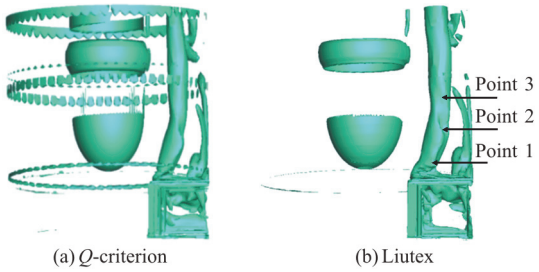

Fig. 10 (Color online) Comparison of the two vortex identification methods in the static domain

Figure 10 shows that no obvious discontinuity occurs at the interface. It also shows that setting the rotation domain will causes errors in the calculation and identification of vortices in numerical simulation. Compared with Fig. 9, the vortex shape obtained here is slightly different. When there is no rotating blade effect, the vortex twists less horizontally. The results of the two vortex recognition criteria are consistent, while the visual field provided by the Liutex method is clearer because it does not have a shear vortex at the sidewall.

4.2 *Interference between the impeller and vortex*

From the previous analysis, the shape of the vortex changes with rotation of the blade. To further reveal the cause of this change, based on the F_2, F_3 results, a plane is taken at $0.3D$ in front of the impeller center, and the vortex change diagram is obtained based on the Q - criterion and Liutex. The two-dimensional streamlines of this plane are obtained, as shown in Fig. 11.

Figures 11(a), 11(b) shows that the vortex positions obtained by the two methods are consistent, but the shapes of the vortex are slightly different. Figures 11(c), 11(d) shows that with the influence of the impeller, the difference in the vortex shape obtained by the two identification methods increases, and more weak vortices can be identified by the Liutex method. Figures 11(e), 11(f) shows that the strong vortices rotate counterclockwise, while the weak vortices near the sidewall rotate clockwise. The streamline in Fig. 11(e) is only affected by the vortex, while the streamline in Fig. 11(f) is affected by both the impeller and vortex. Both vortex identification methods and streamline diagrams show that the rotation of the impeller weakens one vortex and enhances the other.

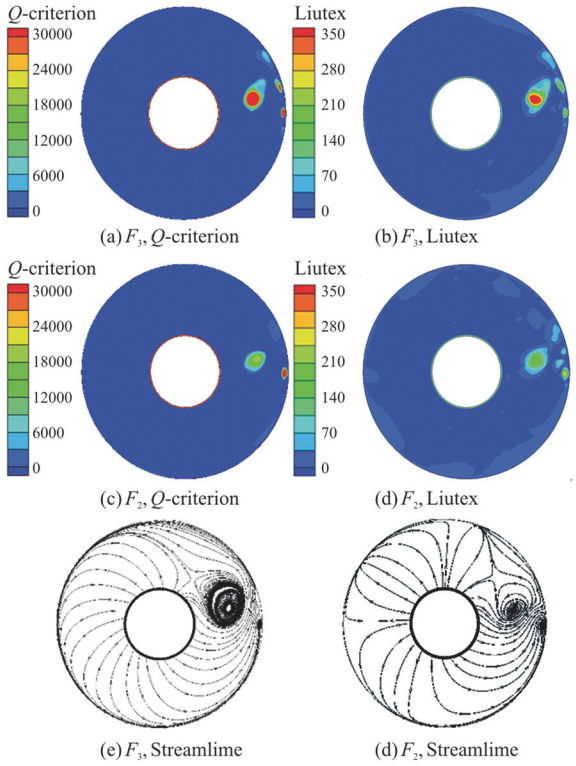

Fig. 11 (Color online) Comparison of vortex identification before the impeller

To analyze the influence of the vortex on the flow field in the impeller and compare the recognition performance of the two vortex identification methods in the rotating impeller, the vortex based on the F_1 and F_2 results is shown in Fig. 12.

Figures 12(a), 12(b) shows that there are complex channel vortices in the impeller even without an inlet vortex. The vortex distributions in each channel are consistent. At the side near the shroud, tip cavitation vortices appear at the blade head, and trace vortices appear at the blade tail. Figures 12(c), 12(d) shows that the inlet vortex occupies approximately one-third of the space in a single channel, and it also affects the tip cavitation vortex and trace vortex. Due to the high-speed rotation of the impeller, the strength of the inlet vortex is weaker than that of the channel vortex. The results of the two vortex identification methods are slightly different in the impeller. The Liutex method can identify the detailed structure of vortices in the rotating impeller.

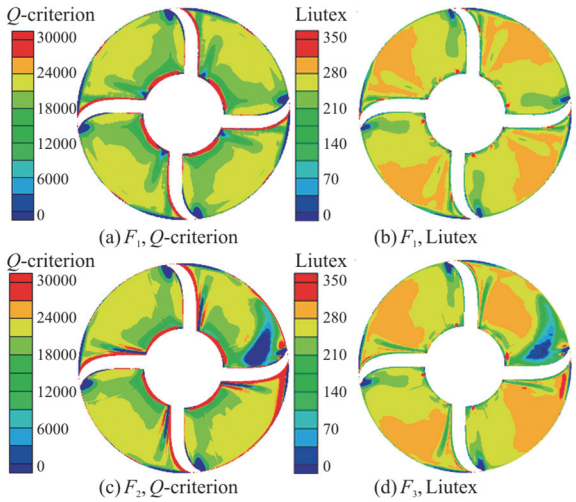

Fig. 12 (Color online) Comparison of vortex identification results in the impeller

4.3 *Influence of the vortex on pressure*

To quantitatively analyze the influence of the vortex and blade on the pressure fluctuation, three points (as shown in Fig. 10(b)) are inserted inside the vortex of the F_1, F_2 and F_3 schemes, and the pressures at these three points are P_1, P_2 and P_3. Define the interaction pressure between the vortex and impeller (P_{2-1}) as follows

$$P_{2-1} = P_2 - P_1 \tag{15}$$

P_{2-1} and P_3 are transformed by the fast Fourier transformation (FFT) method, and the frequency-domain diagram is shown in Fig. 13. The multiple frequencies (f_n) of the impeller are defined as follows

$$f_n = \frac{60f}{n} = \frac{f}{Fz} \tag{16}$$

where f is the frequency obtained by FFT, Fz is the impeller rotation frequency.

Figure 13 shows that when there is no influence of the impeller, the main frequency of the vortex is a low frequency pressure fluctuation. At monitoring point 1, the amplitude of the main frequency is 355 Pa, and the frequency ranges from 0 Hz to 40 Hz. At monitoring point 2, the amplitude of the main frequency is 670 Pa, and the frequency ranges from 0 Hz to 30 Hz. At monitoring point 3, the amplitude of the main frequency is 508 Pa, and the frequency ranges from 0 Hz to 26 Hz. When the monitoring point is far from the VG, the amplitude of the main frequency pressure fluctuation first increases and then decreases, and the vortex frequency gradually decreases. When there is the influence of a rotating impeller, the main frequencies at the three monitoring points are all the blade frequency. The closer the monitoring point is to the impeller, the greater the amplitude of the main frequency is, and the amplitude of the pressure fluctuation at low frequencies significantly decreases.

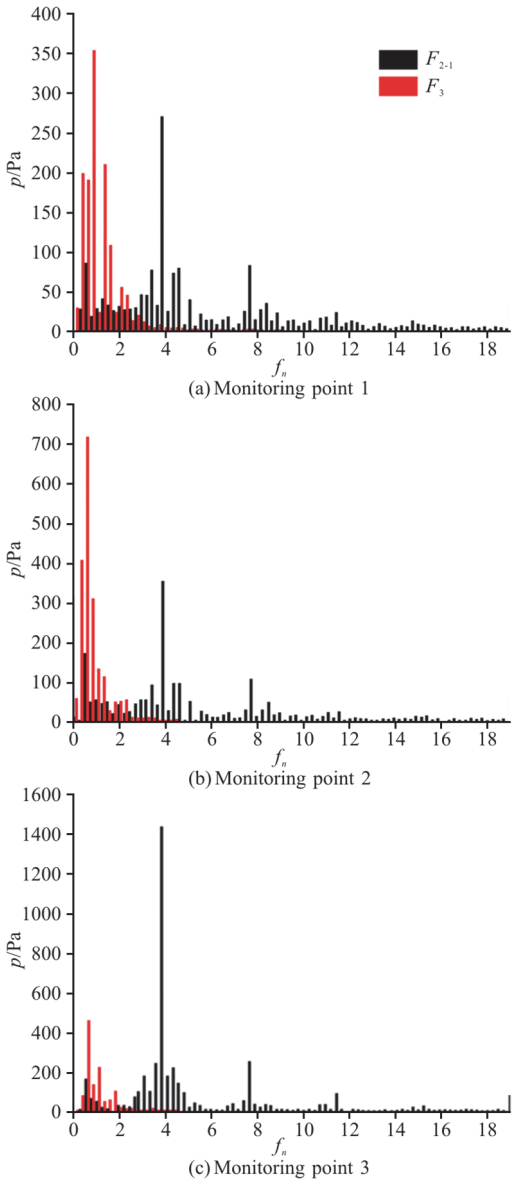

Fig. 13 (Color online) Comparison of pressure fluctuation induced by the vortex

4.4 *Influence of the vortex on velocity*

To study the influence of the vortex on the velocity in the impeller, two points are inserted around the vortex. The velocity vector diagram and the positions of the inserted points are shown in Fig. 14.

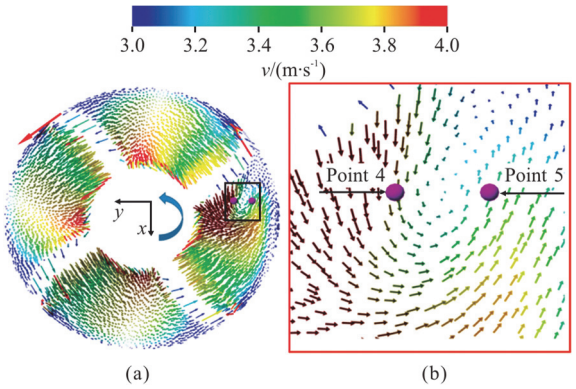

Fig. 14 (Color online) Velocity vector diagram and the monitor point position

The impeller rotates counterclockwise, and the flow velocity vector distribution in the passage not affected by the inlet vortex is consistent. The inlet vortex also rotates in a counterclockwise direction. The direction of the velocity at point 4 is the same as the impeller rotation direction, while the direction of the velocity at point 5 is opposite to the impeller rotation direction.

The tangential velocity is obviously affected by the vortex. To quantitatively analyze the velocity variation due to the vortex in the impeller, the tangential velocities with and without the inlet vortex in the last four periods are taken, as shown in Fig. 15.

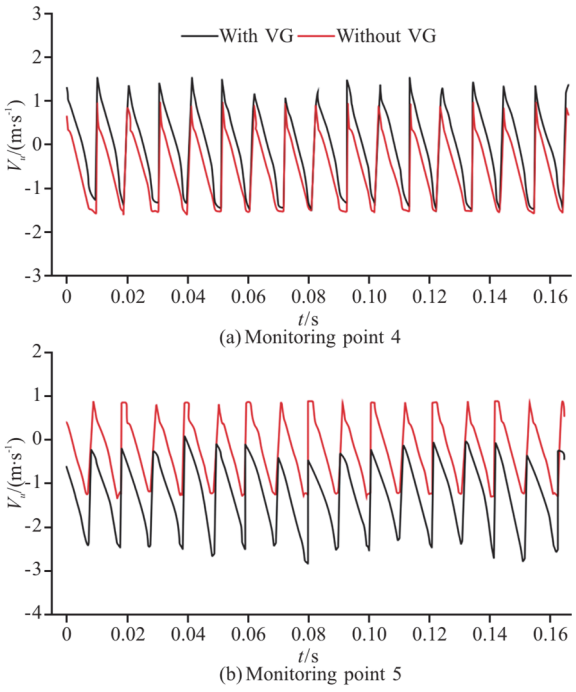

Fig. 15 (Color online) Comparison of the tangential velocity

At point 4, without the VG, the average tangential velocity is –0.47 m/s, and with the VG, the average tangential velocity is 0.07 m/s. At point 5, without the VG, the average tangential velocity is –0.27 m/s, and with the VG, the average tangential velocity is –1.29 m/s. When the vortex velocity at the monitoring point has the same direction as the main flow velocity, the main flow velocity will be increased. In contrast, when the direction of the vortex velocity at the monitoring point is opposite to that of the main flow velocity, the main flow velocity will be decreased. In addition, when vortices occur in the impeller, the periodic changes in velocity are not uniform. The rotation direction of the vortex and its position within the impeller directly influence the monitoring results. Because vortices often exist in pairs, the law of vortex velocity changes in the impeller is worthy of further study.

5. Conclusions

In this paper, both shape and distribution analyses of the vortices in an axial-flow pump based on the Q-criterion and Liutex vortex identification methods are performed. Three different schemes were simulated to analyze the interaction between the impeller and the vortex. The conclusions can be summarized as follows:

(1) For the design flow, the results of the numerical simulation and experiment show that the efficiency error is less than 0.5%, the average axial velocity error along the whole measurement line is small except near both sidewalls. The accuracy of numerical simulations is verified by experiments on the external and internal characteristics.

(2) The results of the two vortex identification methods show that both methods can accurately identify the shape and position of the main vortex. Liutex can not only simultaneously identify strong and weak vortices but also reduce the influence of shear force at the sidewall, which is more suitable for the identification of complex vortices in a rotating impeller.

(3) By installing a flat plate VG, a stable vortex can be continuously generated. In the numerical simulation, the vortex breaks at the dynamic-static interface, which may be caused by data transmission errors.

(4) The vortex and the impeller influence each other. The rotation of the impeller deforms the shape of the inlet vortex. Without a rotating impeller, the main frequency of the pressure pulsation induced by the vortex is a low frequency. With a rotating impeller, the main frequency of the pressure pulsation induced by the vortex is the blade frequency. The vortex significantly changes the tangential velocity inside the impeller.

Acknowledgements

This work was supported by the Natural Science Foundation of Jiangsu Province (Grant No. BK20190914), the China Postdoctoral Science Foundation (Grant No. 2019M661946), the University Science Research Project of Jiangsu Province (Grant No. 19KJB570002) and the Priority Academic Program Development (PAPD) of Jiangsu Higher Education Institutions. The authors especially thank Prof. Chaoqun Liu and his team, as this work was accomplished using code LiutexUTA, which is released by Chaoqun Liu at the University of Texas at Arlington.

References

[1] Tang X., Wang F., Li Y. et al. Numerical investigation of vortex flows and vortex suppression schemes in a large pumping-station sump [J]. *Proceedings of the Institution of Mechanical Engineers, Part C: Journal of Mechanical Engineering Science*, 2011, 225(6): 1459-1480.

[2] Wang Y., Wang P., Tan X. et al. Research on the non-uniform inflow characteristics of the canned nuclear coolant pump [J]. *Annals of Nuclear Energy*, 2018, 115(5): 423-429.

[3] Zhang W., Tang F., Shi L. et al. Effects of an inlet vortex on the performance of an axial-flow pump [J]. *Energies*, 2020, 13(11): 2854.

[4] Rajendran V. P., Constantinescu S. G., Patel V. C. Experimental validation of numerical model of flow in pump-intake bays [J]. *Journal of Hydraulic Engineering, ASCE*, 1999, 125(11): 1119-1125.

[5] Kim C. G., Kim B. H., Bang B. H. et al. Experimental and CFD analysis for prediction of vortex and swirl angle in the pump sump station model [J]. *IOP Conference Series: Materials Science and Engineering*, 2015, 72(4): 042044.

[6] Song X., Liu C. Experimental investigation of floor-attached vortex effects on the pressure pulsation at the bottom of the axial flow pump sump [J]. *Renewable Energy*, 2020, 145: 2327-2336.

[7] Godard G., Stanislas M. Control of a decelerating boundary layer. Part 1: Optimization of passive vortex generators [J]. *Aerospace Science and Technology*, 2006, 10(3): 181-191.

[8] Hansen M. O. L., Charalampous A., Foucaut J. M. et al. Validation of a model for estimating the strength of a vortex created from the bound circulation of a vortex generator [J]. *Energies*, 2019, 12(14): 2781.

[9] Zeng Z., Du P., Wang Z. et al. Combustion flow in different advanced vortex combustors with/without vortex generator [J]. *Aerospace Science and Technology*, 2019, 86(3): 640-649.

[10] Tian X., Zheng Y., Pan H. et al. Numerical and experimental study on a model draft tube with vortex generators [J]. *Advances in Mechanical Engineering*, 2013, 5: 509314.

[11] Tian X., Pan H., Hong S. et al. Improvement of hydro-turbine draft tube efficiency using vortex generator [J]. *Advances in Mechanical Engineering*, 2015, 7(7): 1-8.

[12] Hunt J. C. R., Wray A. A., Moin P. Eddies, stream, and convergence zones in turbulent flows [R]. Proceeding of the Summer Program in Center for Turbulence Research, 1988, 193-208.

[13] Liu C., Wang Y. Q., Yang Y. et al. New omega vortex identification method [J]. *Science China Physics Mechanics and Astronomy*, 2016, 59(8): 56-64.

[14] Wang Y. Q., Gao Y. S., Xu H. et al. Liutex theoretical system and six core elements of vortex identification [J]. *Journal of Hydrodynamics*, 2020, 32(2): 197-211.

[15] Zhang Y. N., Liu K. H., Li J. W. et al. Analysis of the vortices in the inner flow of reversible pump turbine with the new omega vortex identification method [J]. *Journal of Hydrodynamics*, 2018, 30(3): 463-469.

[16] Zhang Y. N., Qiu X., Chen F. P. et al. A selected review of vortex identification methods with applications [J]. *Journal of Hydrodynamics*, 2018, 30(5): 767-779.

[17] Attiya B., Liu I., Altimemy M. et al. Vortex identification in turbulent flows past plates using the Lagrangian method [J]. *Canadian Journal of Physics*, 2019, 97(8): 895-910.

[18] Liu J., Liu C. Modified normalized Rortex/vortex identification method [J]. *Physics of Fluids*, 2019, 31(6): 061704.

[19] Xu S., Long X., Ji B. et al. Vortex dynamic characteristics of unsteady tip clearance cavitation in a waterjet pump determined with different vortex identification methods [J]. *Journal of Mechanical Science and Technology*, 2019, 33(12): 5901-5912.

[20] Wang Y. Q., Gui N. A review of the third-generation vortex identification method and its applications [J]. *Chinese Journal of Hydrodynamics*, 2019, 34(4): 413-429(in Chinese).

[21] Gao Y., Liu C. Rortex and comparison with eigenvalue-based vortex identification criteria [J]. *Physics of Fluids*, 2018, 30(8): 085107.

[22] Liu C., Gao Y., Tian S. et al. Rortex-A new vortex vector definition and vorticity tensor and vector decompositions [J]. *Physics of Fluids*, 2018, 30(3): 035103.

[23] Liu C. Letter: Galilean invariance of Rortex [J]. *Physics of Fluids*, 2018, 30(11): 111701.

[24] Wang Y. F., Zhang W. H., Cao X. et al. The applicability of vortex identification methods for complex vortex structures in axial turbine rotor passages [J]. *Journal of Hydrodynamics*, 2019, 31(4): 700-707.

[25] Smirnov P. E., Menter F. R. Sensitization of the SST turbulence model to rotation and curvature by applying the Spalart-Shur correction term [J]. *Journal of Turbomachinery*, 2009, 131(4): 041010.

[26] Chitrakar S., Thapa B. S., Dahlhaug O. G. et al. Numerical and experimental study of the leakage flow in guide vanes with different hydrofoils [J]. *Journal of Computational Design and Engineering*, 2017, 4(3): 218-230.

[27] Liu Y., Zhong L., Lu L. Comparison of DDES and URANS for unsteady tip leakage flow in an axial compressor rotor [J]. *Journal of Fluids Engineering*, 2019, 141(12): 121405.

[28] Shi L., Zhang W., Jiao H. et al. Numerical simulation and experimental study on the comparison of the hydraulic characteristics of an axial-flow pump and a full tubular pump [J]. *Renewable Energy*, 2020, 153: 1455-1464.